Supporting Information

Engineering Pore Size of Interpenetrated Metal-Organic Frameworks for Molecular Sieving Separation of C_2H_2/C_2H_4

Pengxiang Wang†[1], Shuangqing Shang†[1], Hanting Xiong[1], Xing Liu[1], Junhui Liu[1], Hua Shuai[1], Lingmin Wang[1], Zhenglong Zhu[1], Zhiwei Zhao[1], Yong Peng[1], Jingwen Chen[1], Shixia Chen[1], Zhenyu Zhou[1]*, Jun Wang[1]

1. Chemistry and Chemical Engineering School, Nanchang University, Nanchang, Jiangxi 330031, China

2. School for Engineering of Matter, Transport and Energy, Arizona State University, Tempe, Arizona 85287, United States

†These authors contributed equally to this work

*Corresponding author.

E-mail addresses: zhouzhenyu@ncu.edu.cn (Z. Zhou)

Materials and methods

1. Materials

Zinc nitrate hexahydrate ($Zn(NO_3)_2 \cdot 6H_2O$, 99.99%, Aladdin), 4,4'-Sulfonylbis(benzoic acid) (SDBA, 96%, Leyan), 4,4'-Vinylenedipyridine (dpe, 98%, Macklin), 4,4'-Bipyridine (bpy, 98%, Macklin), methanol (CH_3OH, anhydrous, 99.9%, Aladdin), N,N-Dimethylformamide (DMF, 99.8%, Aladdin), were commercially available and used without further purification. N_2 (99.999%), C_2H_2 (99.99%), C_2H_4 (99.99%), He (99.999%), and mixed gases of C_2H_2/C_2H_4 (1/99, *v/v*) and C_2H_2/C_2H_4 (1/99, *v/v*) were purchased from Nanchang Jiangzhu Gas Co., Ltd (China).

2. Characterization

Powder X-ray diffraction (PXRD) patterns were collected on a PANalytical Empyrean Series 2 diffractometer with Cu Kα radiation (λ = 1.540598 Å), which was operated at 40 kV, 40 mA with a scan speed of 0.0167°, a scan time of 15 s per step, and 2θ ranging from 5 to 60° at room temperature. The thermogravimetric analysis (TGA) was performed on a NETZSCH Thermogravimetric Analyzer (STA2500) from 30 to 800 °C with a heating rate of 10 °C min^{-1} under N_2 atmosphere. The single-component adsorption isotherms of C_2H_2, C_2H_4 at 298, 308, and 318 K were collected on Micromeritics 3-Flex adsorption apparatus. The degassing procedure for all samples was carried out at 373 K under vacuum for 24 h before each adsorption measurement. The Brunauer-Emmett-Teller (BET) specific surface area was calculated based on the CO_2 adsorption isotherms (relative pressure: 0.05-0.15) at 195 K. The pore size distribution (PSD) was derived from the adsorption branch of CO_2 adsorption isotherms using the non-local density functional theory (NLDFT) method and assuming a slit pore model.

3. Experimental

3.1 Synthesis of Zn-SDBA-dpe

$Zn(NO_3)_2 \cdot 6H_2O$ (180 mg), dpe (108 mg) , SDBA (200.6 mg) were added to 20 ml of DMF and 20 ml of methanol and stirred for 30 min to mix well, and when it is completely dissolved, transfer the mixed solution to 100 ml of PTFE inner tank, then put into the reactor and sealed. Put the reactor into an oven at 120 °C, maintain the

reaction at 120 °C for 72 h, and remove the reactor after cooling to room temperature. The mother liquor was collected by centrifugation (10000 rpm, 8 min) and the samples were washed three times each with DMF and methanol, respectively. After soaking in methanol solution for three days, changing to a new methanol solution every day, and finally vacuum drying at 373 K to obtain activated Zn-SDBA-dpe white powder.

3.2 Synthesis of Zn-SDBA-bpy

$Zn(NO_3)_2 \cdot 6H_2O$ (180 mg), bpy (93.71 mg), SDBA (200.6 mg) were added to 20 ml of DMF and 20 ml of methanol and stirred for 30 min to mix well, and after it was completely dissolved, the mixed solution was transferred to 100 ml of PTFE inner tank, and then put into the reactor and sealed. The reactor was placed in an oven at 120 °C for 72 h, then removed and cooled to room temperature. The resulting mother liquor was filtered, washed with DMF and methanol three times each, then soaked in methanol solution for three days, replaced with a new methanol solution every day, and finally vacuum dried at 373 K to obtain activated Zn-SDBA-bpy white microcrystalline powder.

4. Calculations based on single competent isotherms

Gas adsorption isotherms of C_2H_2 and C_2H_4 on Zn-SDBA-dpe and Zn-SDBA-bpy were fitted with the Dual-Site Langmuir-Freundlich isotherm model:

$$N = A_1 \times \frac{B_1 \times P^{C_1}}{1 + B_1 \times P^{C_1}} + A_1 \times \frac{B_1 \times P^{C_1}}{1 + B_1 \times P^{C_1}} \quad (1)$$

Where N is molar loading of adsorbents (mmol g^{-1}), A_1 and A_2 are saturation capacity of site 1 and site 2 (mmol g^{-1}), B_2 and B_2 are affinity coefficients of site 1 and site 2 (kPa^{-C}), C_1 and C_2 represent the deviations from an ideal homogeneous surface, and P is bulk gas phase pressure at equilibrium with the adsorption phase (kPa).

The adsorption selectivity for the mixture C_2H_2/C_2H_4 are defined by

$$S_{ads} = \frac{x_1 / x_2}{y_1 / y_2} \quad (2)$$

Where S_{ads} is adsorption selectivity, x_1 and x_2 are the molar fraction of component in the adsorbed phases in equilibrium with the bulk gas phase, and y_1 and y_2 is mole

fractions of component in the bulk phases.

The experimental adsorption enthalpy (Q_{st}) was applied to evaluate the binding strength between adsorbent and adsorbate. The adsorption heat of each component was determined precisely according to the virial fitting parameters of single-component gas adsorption isotherms measured at 298, 308, and 318 K up to 1.0 bar, which was defined as follows:

$$\ln p = \ln N + \frac{1}{T}\sum_{i=0}^{m} a_i N^i + \sum_{i=0}^{n} b_i N^i \tag{4}$$

$$Q_{st} = -R\sum_{i=0}^{m} a_i N^i \tag{5}$$

where P is pressure (mmHg), N is the amount adsorbed (mg/g), T is temperature (K), and m and n are the numbers of coefficients required to adequately describe the isotherms. The Q_{st} was calculated by the Clausius-Clapeyron equation and was defined as

$$Q_{st} = -R^2\left(\frac{\partial \ln P}{\partial T}\right)$$

5. Simulated detail

The binding energy was calculated by first-principles density functional theory (DFT) in combination with plane-wave Ultrasoft pseudopotential implemented in the Material Studio, CASTEP code. Calculations were performed under the generalized gradient approximation with the Perdew-Burke-Ernzerhof (PBE) exchange-correlation. The cutoff energy of 561 eV and 2 × 2 × 1 k-point mesh was found to be enough for the total energy to converge within 0.1 meV atom^{-1}. First, the structure of Zn-SDBA-dpe and Zn-SDBA-bpy were optimized to well match with the experimentally determined crystal structure. Various gas guest molecules were then optimized and added to various locations of the channel pore, followed by a full structural relaxation. The static binding energy (at T = 0 K) was then calculated using ΔE = E(MOF) + E(gas) - E(MOF + gas).

The diffusion barrier calculation uses the transition state search task in the CASTEP code, and the parameters related to electron interaction are the same as those

of the site calculation. The diffusion barrier is obtained by calculating the migration trajectory energy between adjacent sites, and frequency analysis confirms the correctness of the transition state.

6. Rietveld refinement of PXRD

The Rietveld refinements of different XRD patterns were performed using the TOPAS academic program. The single crystal structures of Zn-SDBA-bpe and Zn-SDBA-bpy were taken as the original crystal models. The background, scale factor, zero, cell parameters, and profile parameters, such as U, V, and W of the Pseudo-Voigt function, were refined. Additionally, the atomic positions of Zn and S were also refined until convergence was achieved.

7. Breakthrough experiments

The dynamic breakthrough experiment was carried out on a home-made apparatus **(Figure S35)**. Typically, the activated Zn-SDBA-bpy (0.8413 g) and Zn-SDBA-dpe (0.9874 g) was packed into a stainless-steel column (4.6mm inner diameter × 240 mm). The column was first purged with a He flow (10 mL min^{-1}) at room temperature for 8 h before breakthrough measurements. For C_2H_2/C_2H_4 (1/99) and C_2H_2/C_2H_4 (50/50), the gas-mixture was introduced at a flow rate of 2.0 mL min^{-1}. The outlet gas from the column was monitored using gas chromatography (GC-490 plus) with a flame ionization detector. After the breakthrough measurement, the columns packed with samples were regenerated by purging dry He gas (2 mL min^{-1}) at 100 °C for 10 h. The outlet composition during desorption was continuously monitored by a mass spectrometer or gas chromatography until a complete regeneration was achieved.

8. Calculations of separation factor (α)

The amount of adsorbed gas *i* (q_i) was calculated from the breakthrough curve as follows

$$q_i = \frac{C_i V}{22.4 \times m} \times \int_0^t \left(1 - \frac{F}{F_0}\right) dt$$

Here, C_i is the feed gas concentration, V is the influent flow rate of gas (mL min-1), t is the adsorption time (min), F_0 and F are the inlet and outlet gas molar flow rates, respectively, m is the mass of the sorbent (g).

The separation factor, also known as separation selectivity (α) for the breakthrough experiment, which was determined as follows

$$\alpha = \frac{y_2 q_1}{y_1 q_2}$$

Where y_i is the molar fraction of gas i in the gas mixture, q is the adsorption capacity calculated above.

Supplementary Figures

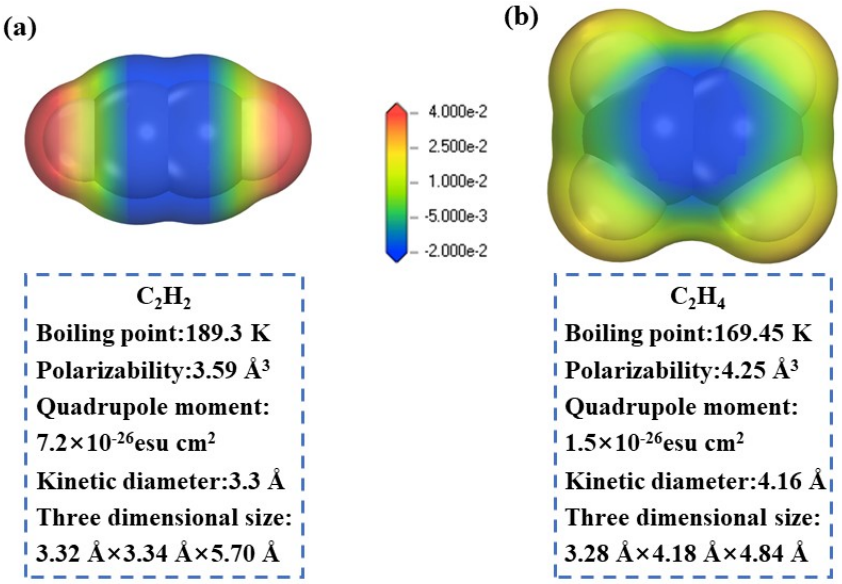

Figure S1. Isosurface maps of the molecular electrostatic potential (MESP), molecular sizes, and physical properties for (a) C_2H_2 and (b) C_2H_4. Red and blue colors represent the positive and negative part of MESP, respectively.

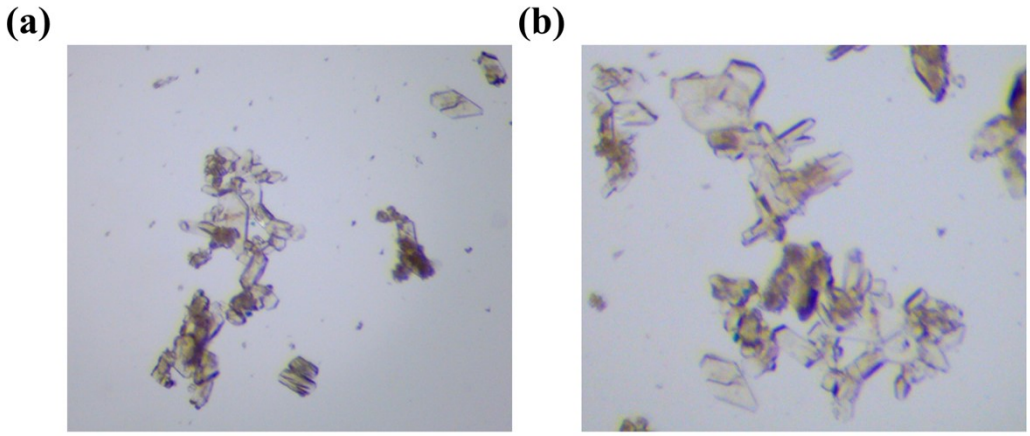

Figure S2. Digital photograph of single-crystal of (a) Zn-SDBA-dpe and (b) Zn-SDBA-bpy.

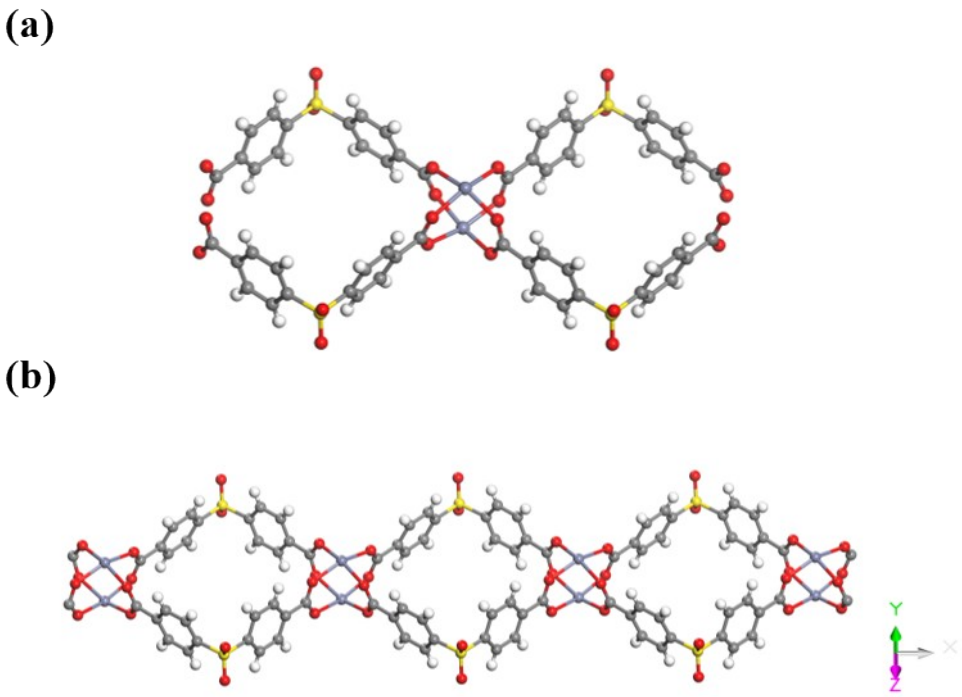

Figure S3. (a) Zn-based secondary building unit (SBU) coordinated with four SDBA ligands. (b) The generating one-dimensional (1D) [Zn(SDBA)]n chains.

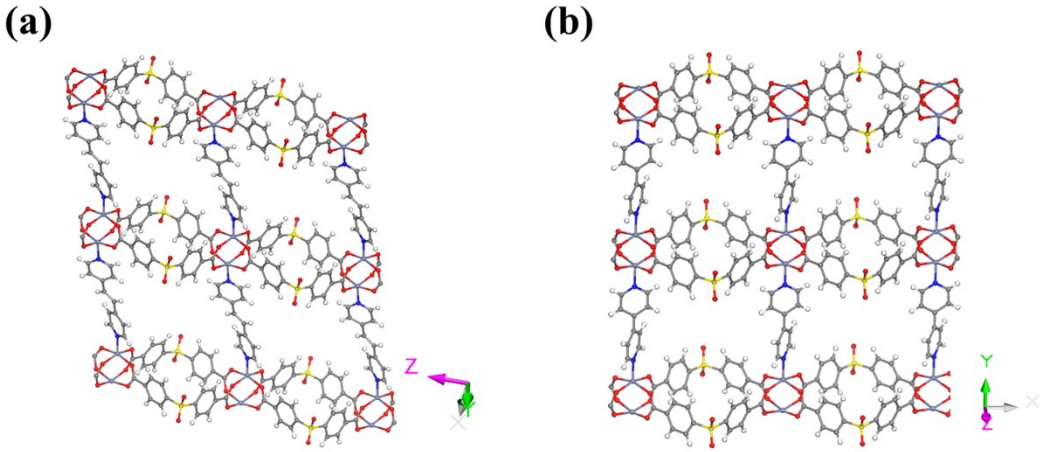

Figure S4. 2D layer structure of (a) Zn-SDBA-dpe and (b) Zn-SDBA-bpy.

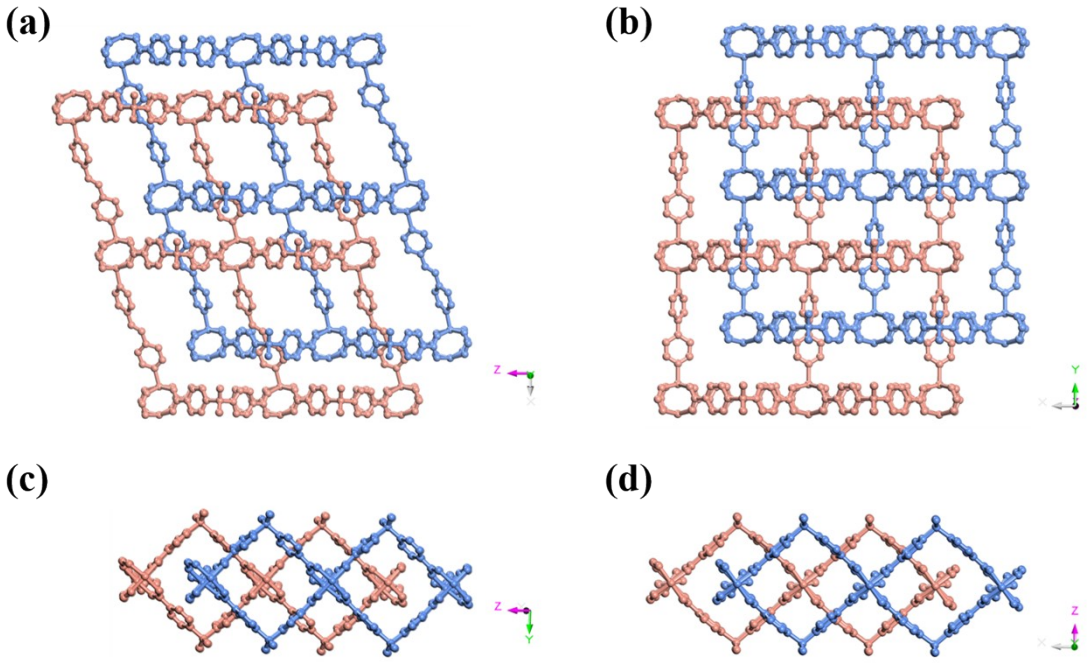

Figure S5. Structural diagrams of two-fold interpenetration of 2D $[Zn\text{-}SDBA\text{-}dpe]_n$ layers along (a) Y-axis direction, (c) X-axis direction, and of 2D $[Zn\text{-}SDBA\text{-}bpy]_n$ layers along (b) Z-axis direction, (d) Y-axis direction.

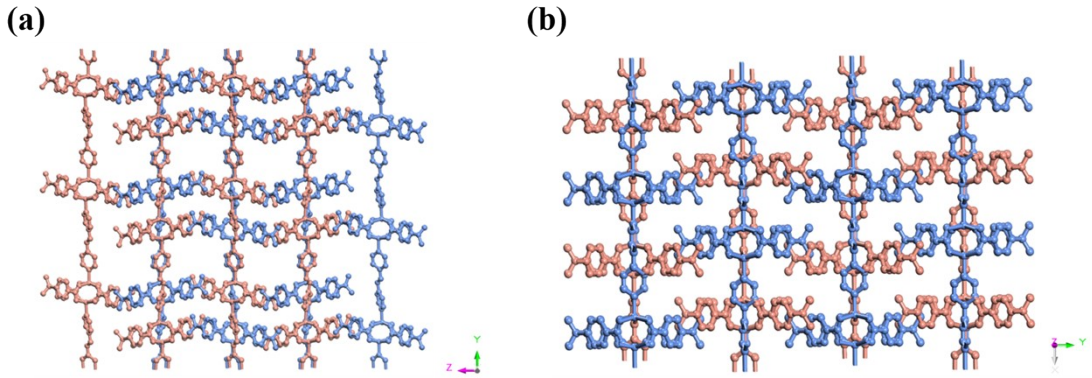

Figure S6. Dual-interpenetrated structure of the 3D (a) Zn-SDBA-dpe framework along X-axis direction and (b) Zn-SDBA-bpy framework along Z-axis direction.

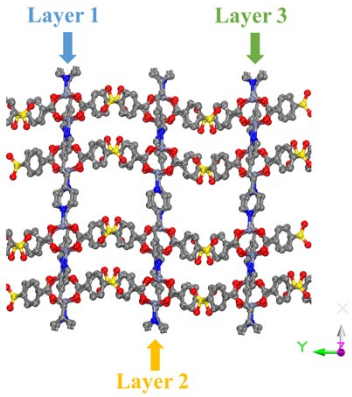

Figure S7. Zn-SDBA-dpe framework along Z-axis direction.

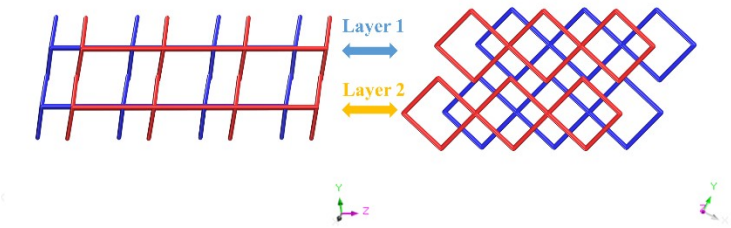

Figure S8. A schematic diagram illustrating the structure of Zn-SDBA-dpe in other directions, with clear labels indicating Layer 1 and Layer 2.

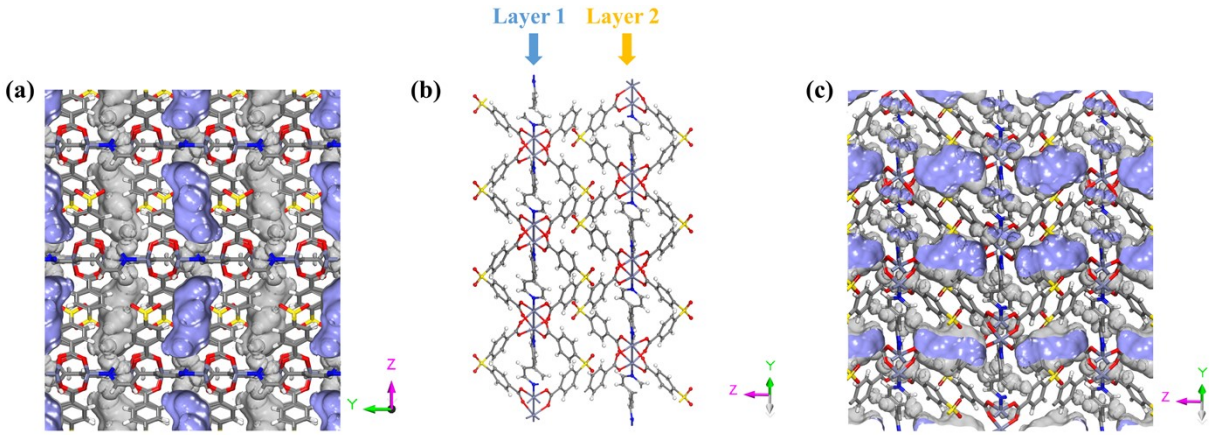

Figure S9. a) Zn-SDBA-bpy framework with interlayer pore channels X-axes. b-c) The angle at which the C_2H_2 molecule enters the framework through the interlayer cavity.

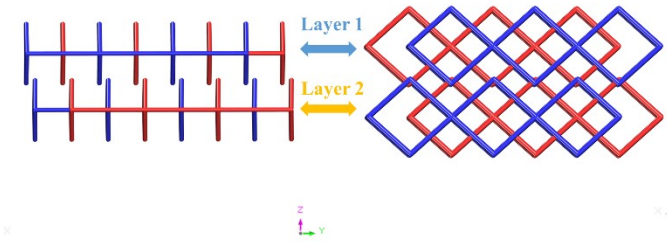

Figure S10. A schematic diagram illustrating the structure of Zn-SDBA-bpy in other directions, with clear labels indicating Layer 1 and Layer 2.

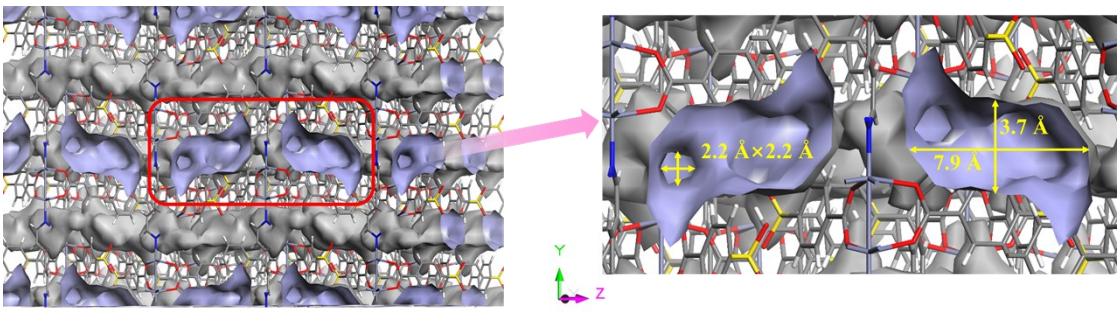

Figure S11. The schematic diagram of the interlayer cavity and pore window of Zn-SDBA-bpy along X-axes. Accessible Connolly surface is determined by a probe with the radius of 1.0 Å.

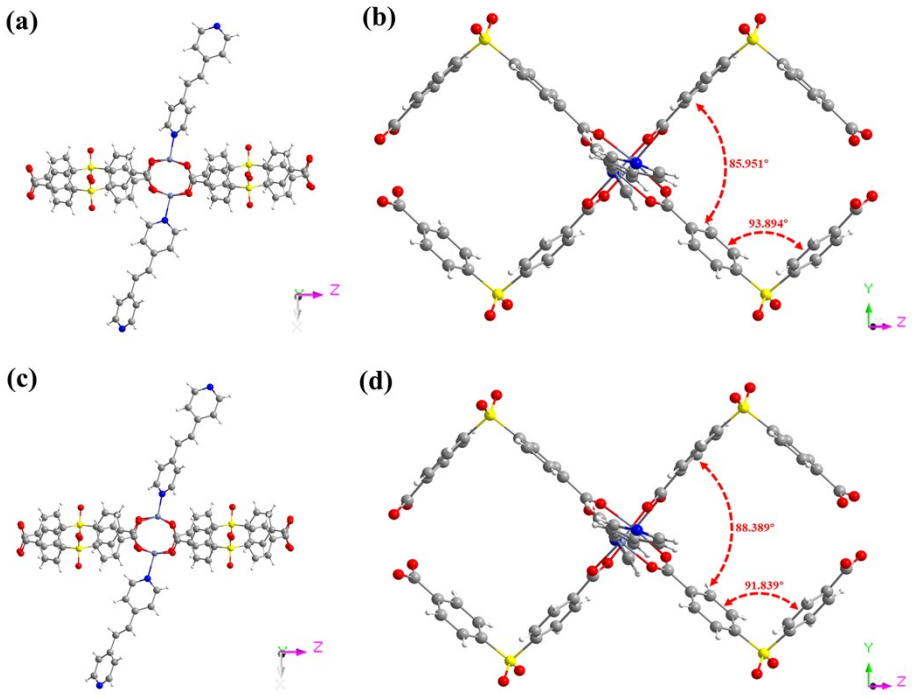

Figure S12. The coordination environment of Zn(II) SBU along the (a) Y-axis direction and (b) X-axis direction of as-synthesized Zn-SDBA-dpe. The coordination environment of Zn(II) SBU along the (c) Y-axis direction and (d) X-axis direction of activated Zn-SDBA-dpe.

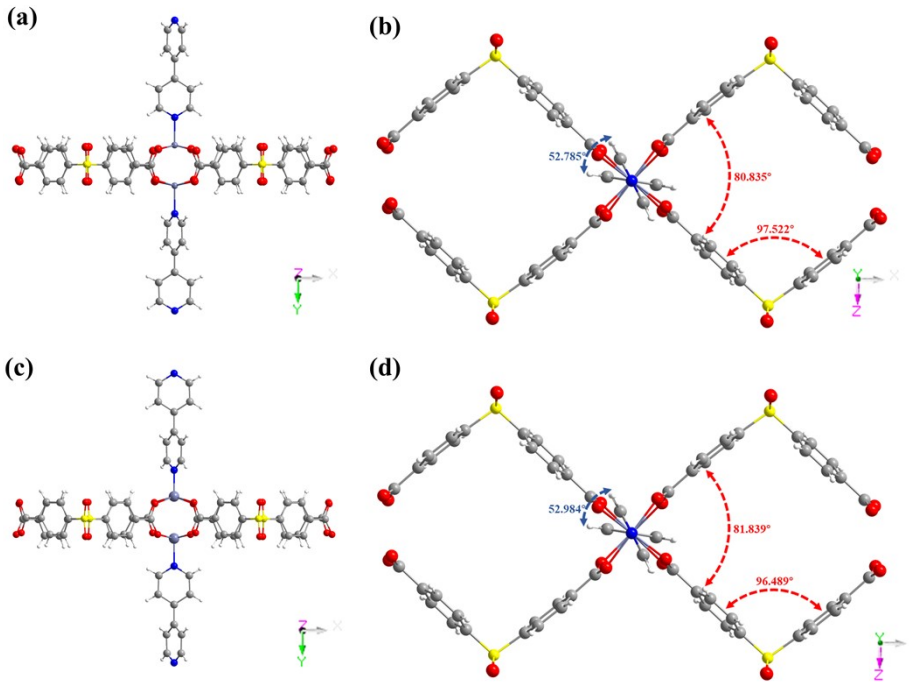

Figure S13. The coordination environment of Zn(II) along the (a) Z-axis direction and (b) Y-axis direction of as-synthesized Zn-SDBA-dpy. The coordination environment of Zn(II) along the (c) Z-axis direction and (d) Y-axis direction of of activated Zn-SDBA-dpy.

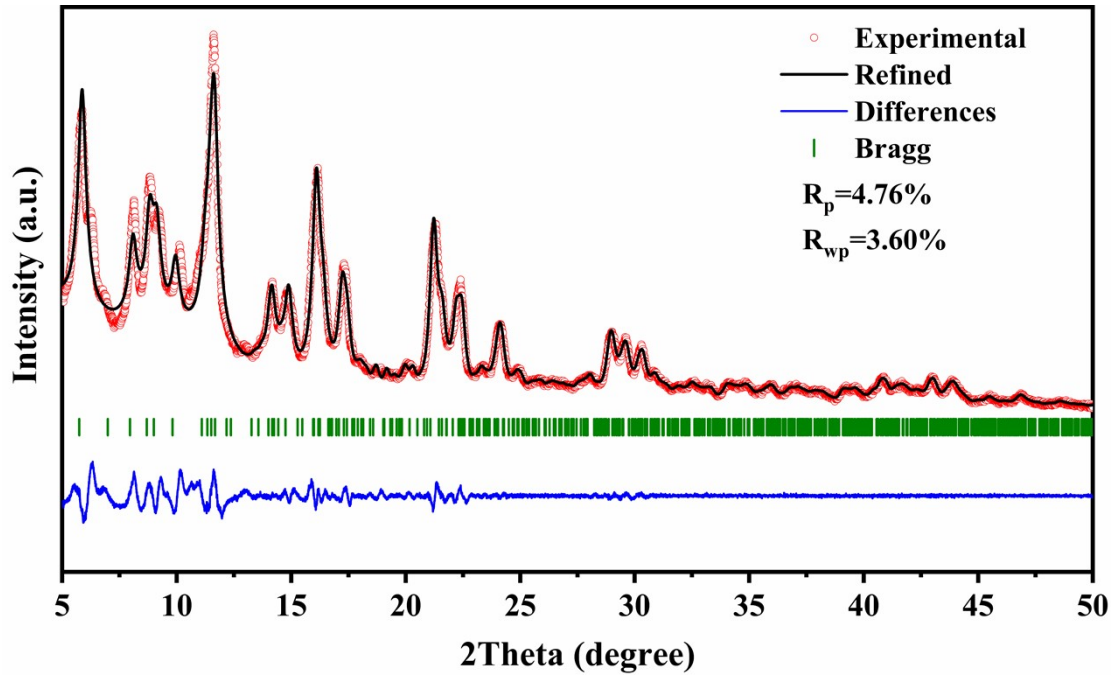

Figure S14. The powder X-ray diffraction Rietveld refinement plot of Zn-SDBA-dpe.

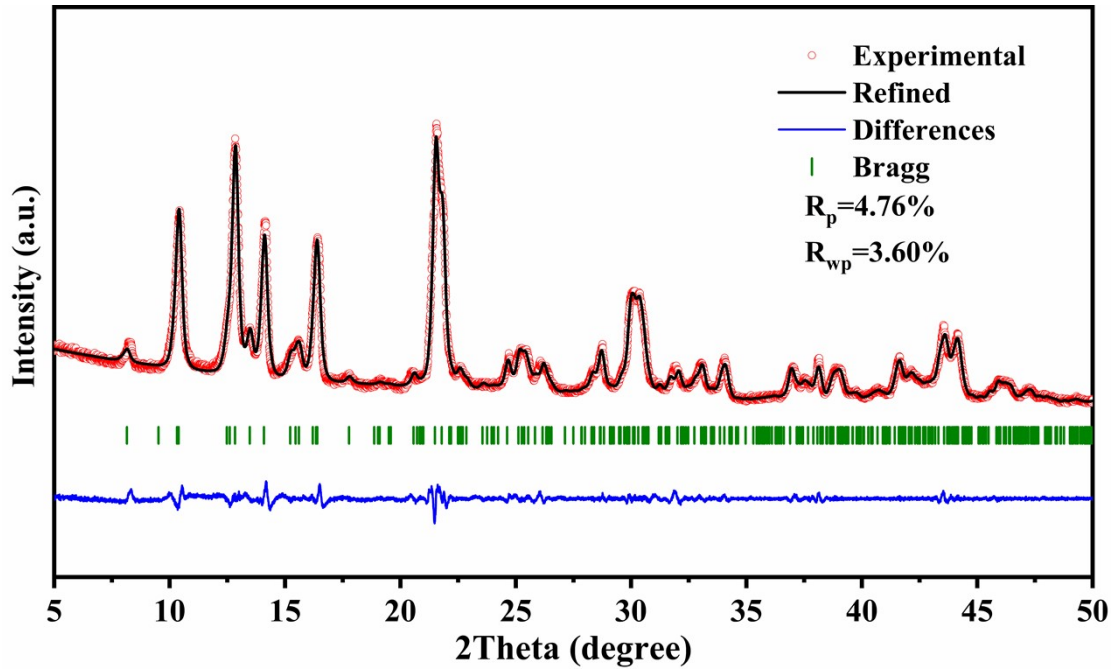

Figure S15. The powder X-ray diffraction Rietveld refinement plot of Zn-SDBA-bpy.

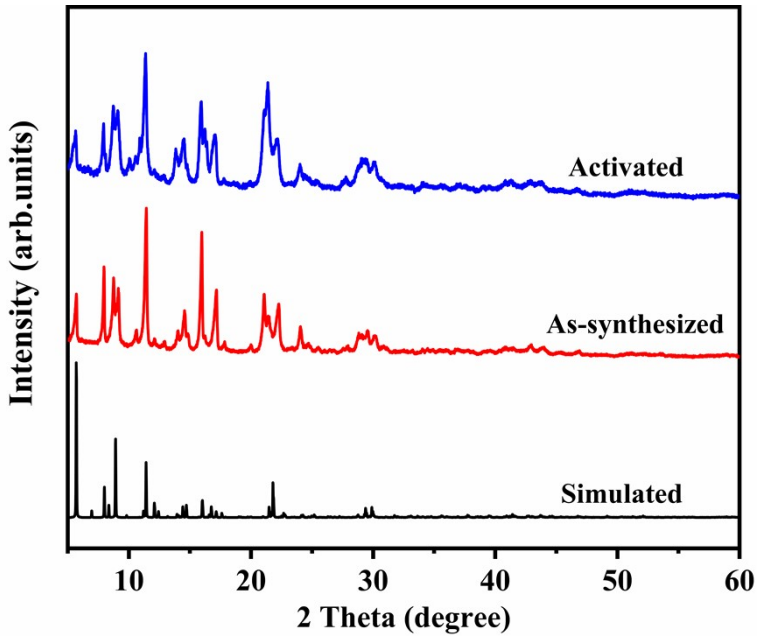

Figure S16. PXRD patterns of Zn-SDBA-dpe under different conditions.

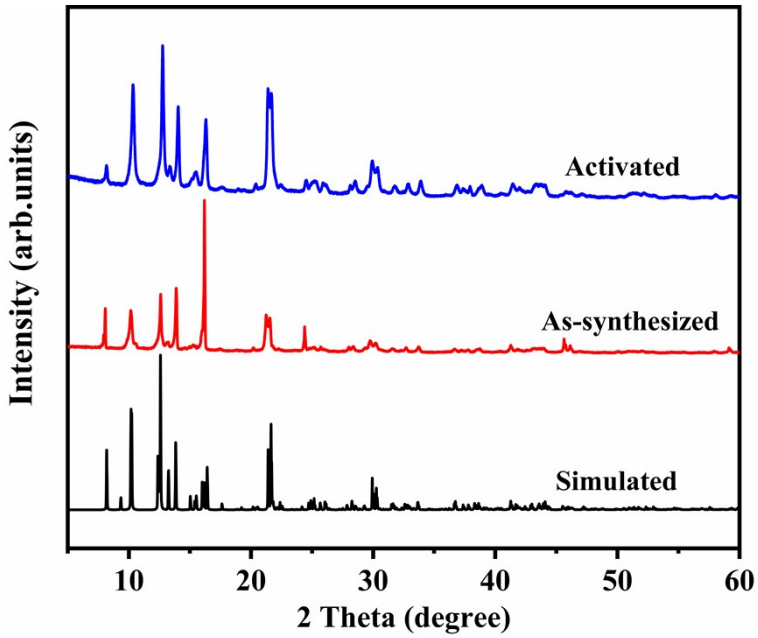

Figure S17. PXRD patterns of Zn-SDBA-bpy under different conditions.

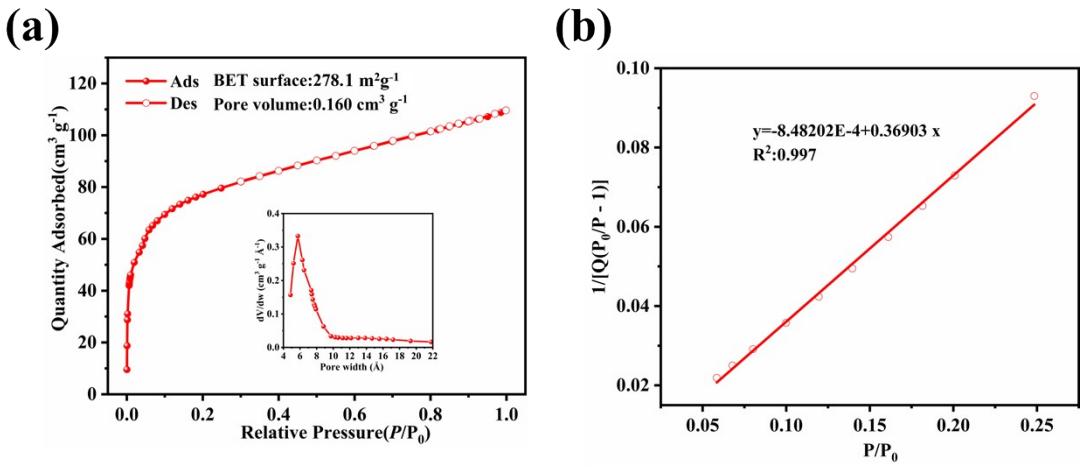

Figure S18. (a) CO_2 adsorption isotherm of Zn-SDBA-dpe at 195 K; (b) BET calculation plot for Zn-SDBA-dpe based on its corresponding CO_2 adsorption isotherm at 195 K.

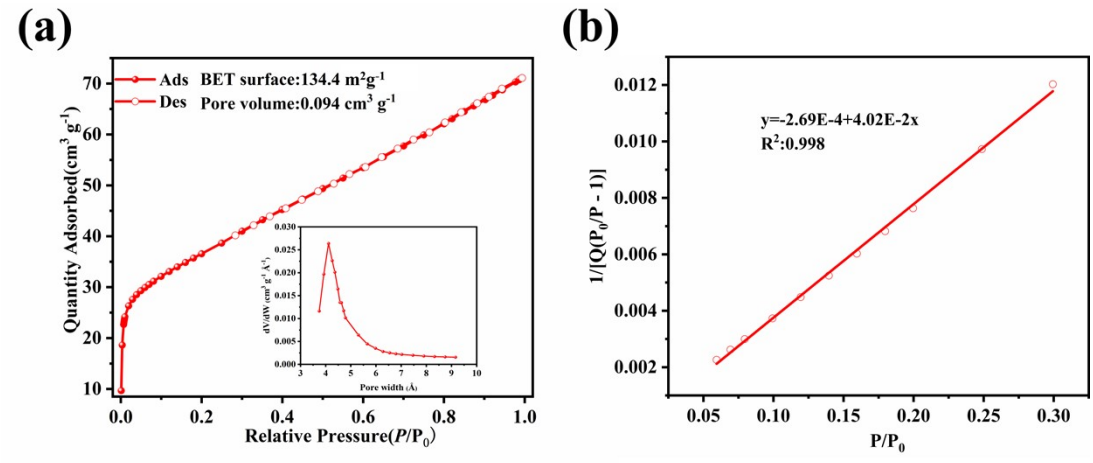

Figure S19. (a) CO_2 adsorption isotherm of Zn-SDBA-bpy at 195 K; (b) BET calculation plot for Zn-SDBA-bpy based on its corresponding CO_2 adsorption isotherm at 195 K.

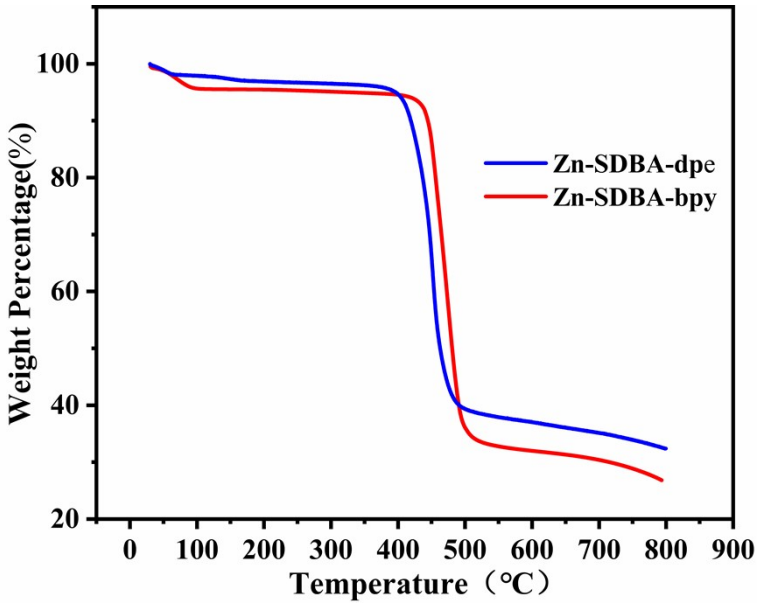

Figure S20. TGA curves of Zn-SDBA-dpe and Zn-SDBA-bpy.

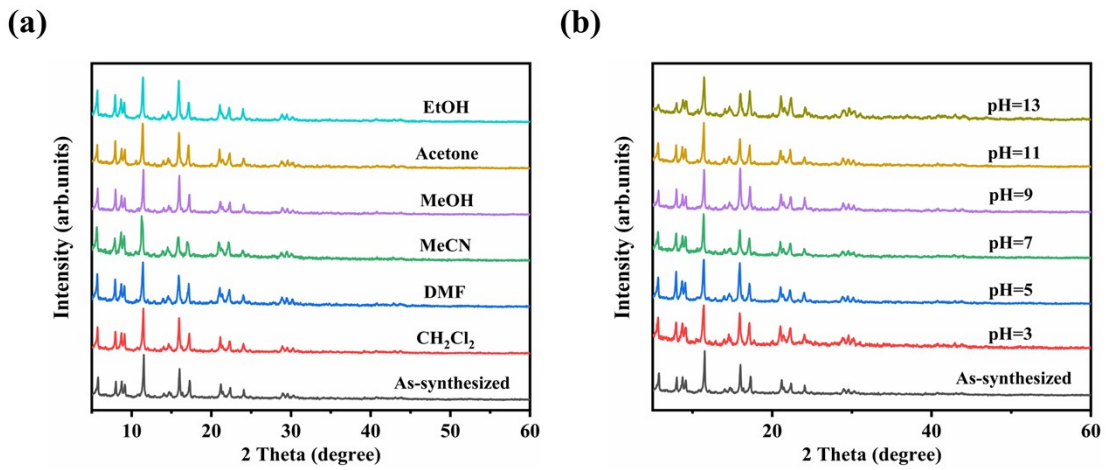

Figure S21. PXRD patterns after treatments. The powder X-ray diffraction patterns of Zn-SDBA-dpe after immersing in (a) different organic solvents for 30 days; (b) acid/basic solutions with different pH for 7 days.

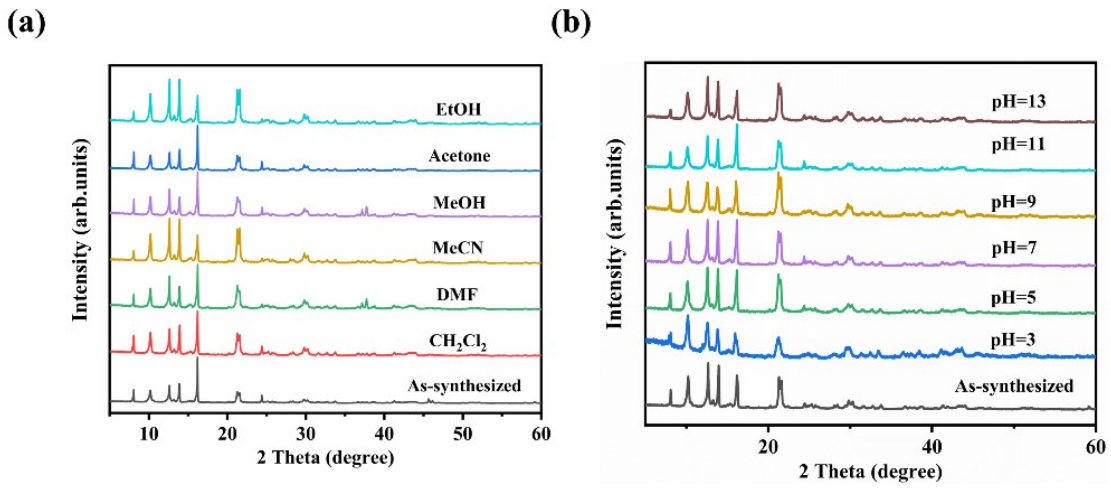

Figure S22. PXRD patterns after treatments. The powder X-ray diffraction patterns of Zn-SDBA-bpy after immersing in (a) different organic solvents for 30 days; (b) acid/basic solutions with different pH for 7 days.

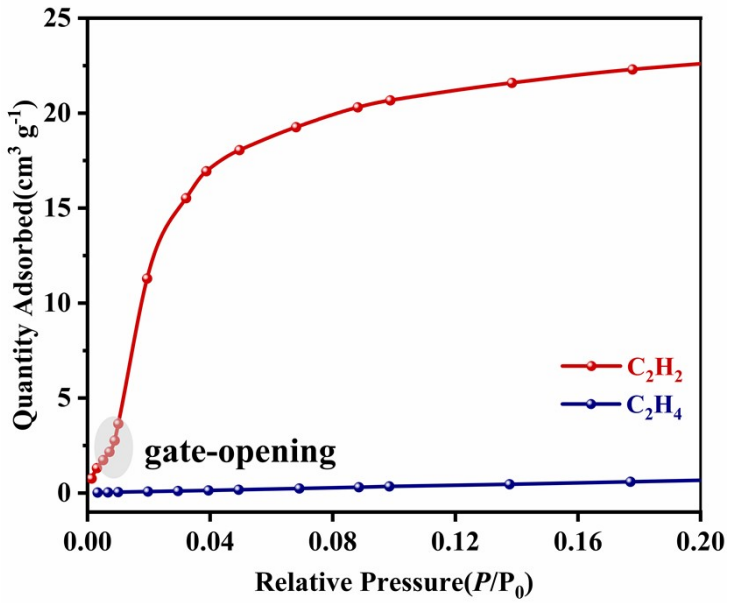

Figure S23. The adsorption capacity of C_2H_2 on Zn-SDBA-bpy under low-pressure conditions.

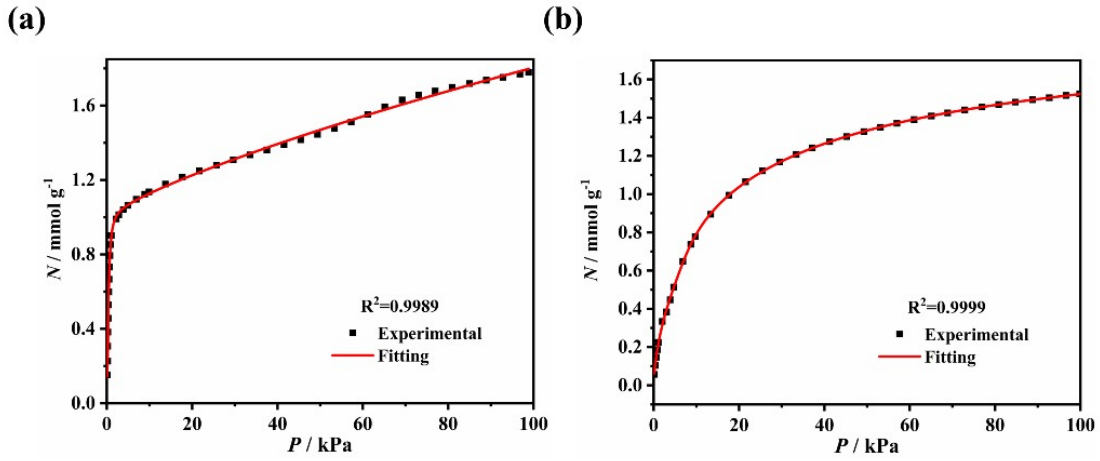

Figure S24. The dual-site Langmuir-Freundlich isotherm model for Zn-SDBA-dpe adsorption isotherms of (a) C_2H_2 and (b) C_2H_4 at 298 K.

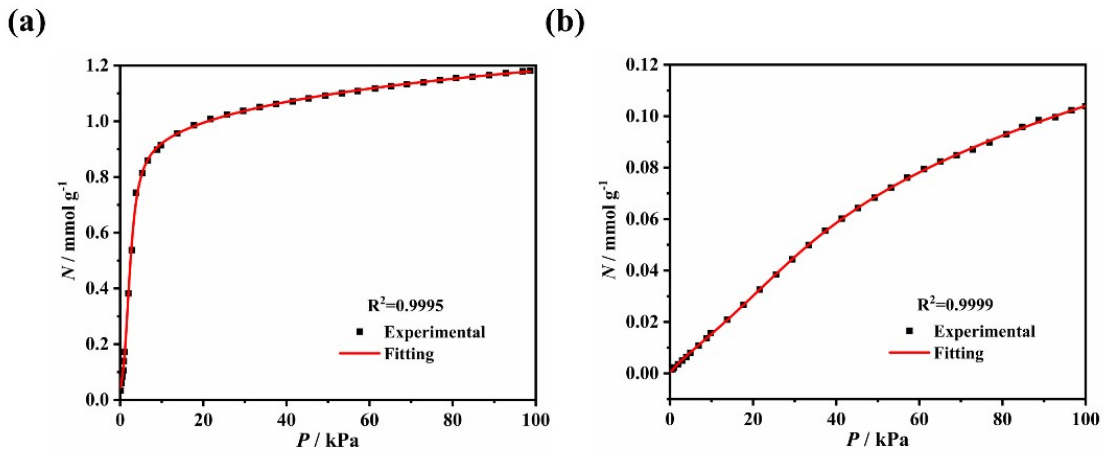

Figure S25. The dual-site Langmuir-Freundlich isotherm model for Zn-SDBA-bpy adsorption isotherms of (a) C_2H_2 and (b) C_2H_4 at 298 K.

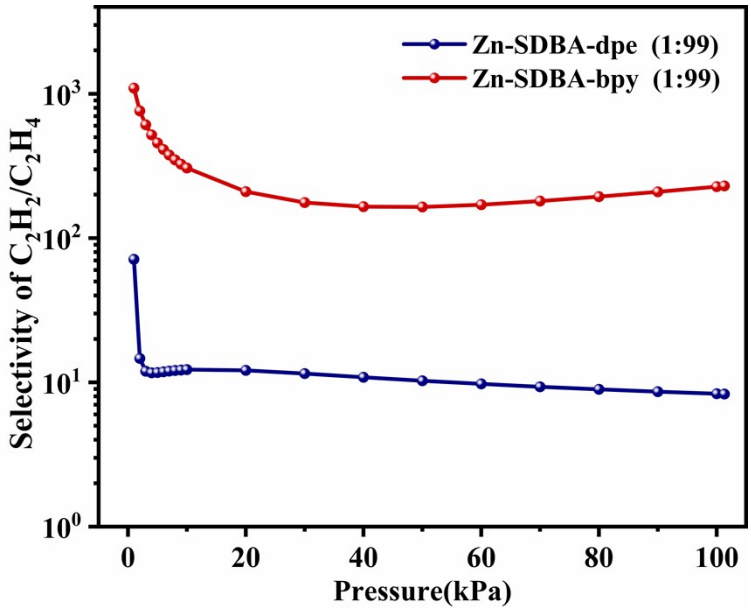

Figure S26. IAST selectivity of C_2H_2/ C_2H_4 (1/99) on Zn-SDBA-dpe and Zn-SDBA-bpy at 298 K.

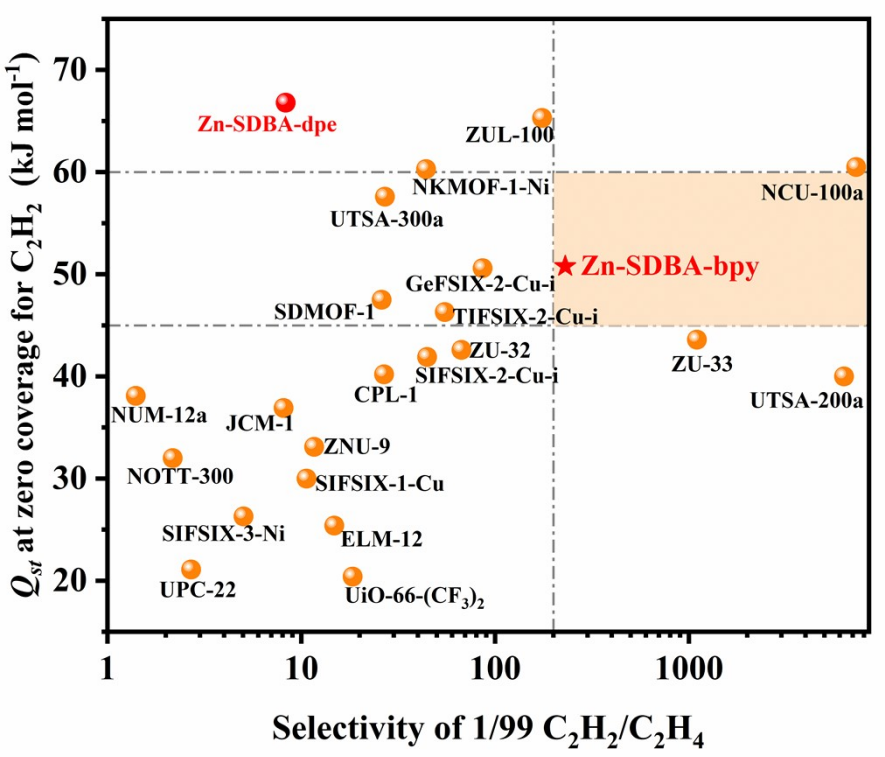

Figure S27. Comparison of the Q_{st} and Selectivity at 1 bar in representative MOFs.

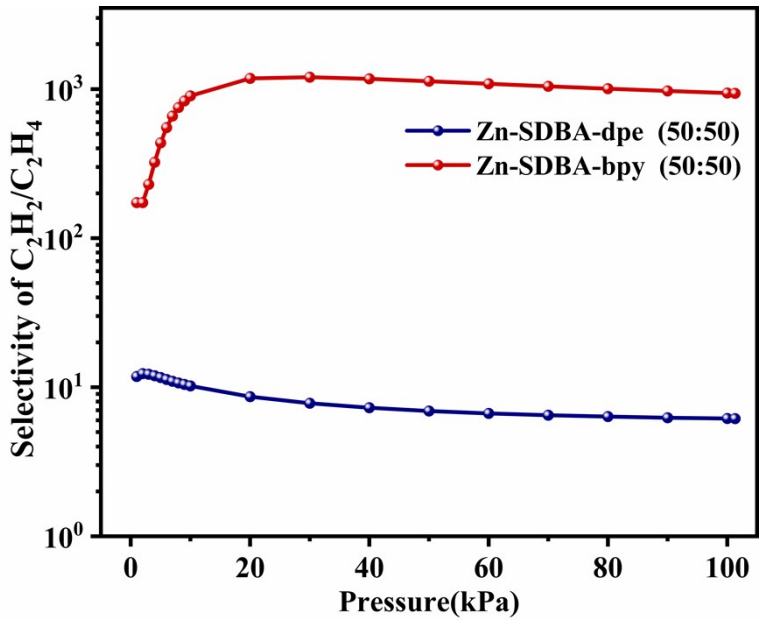

Figure S28. IAST selectivity of C_2H_2/ C_2H_4 (50/50) on Zn-SDBA-dpe and Zn-SDBA-bpy at 298 K.

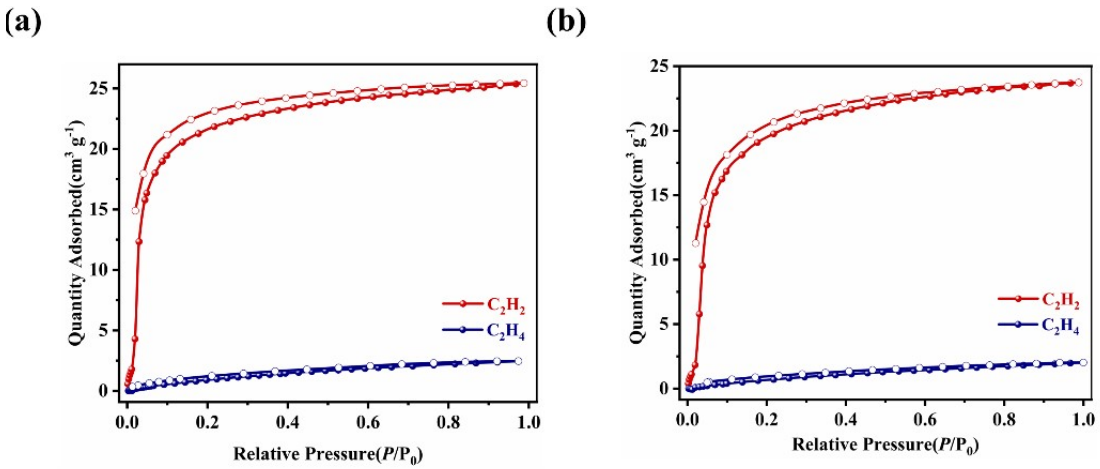

Figure S29. Adsorption isotherms of C_2H_2 and C_2H_4 on Zn-SDBA-bpy at (a) 308 K and (b) 318 K.

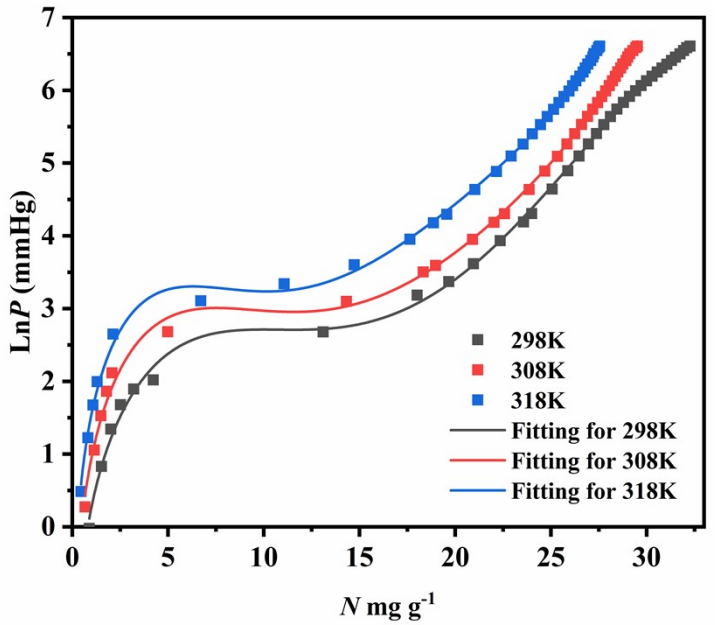

Figure S30. Virial fitting curves for (a) C_2H_2 adsorption isotherms on Zn-SDBA-bpy at 298, 308, and 318 K up to 1 bar.

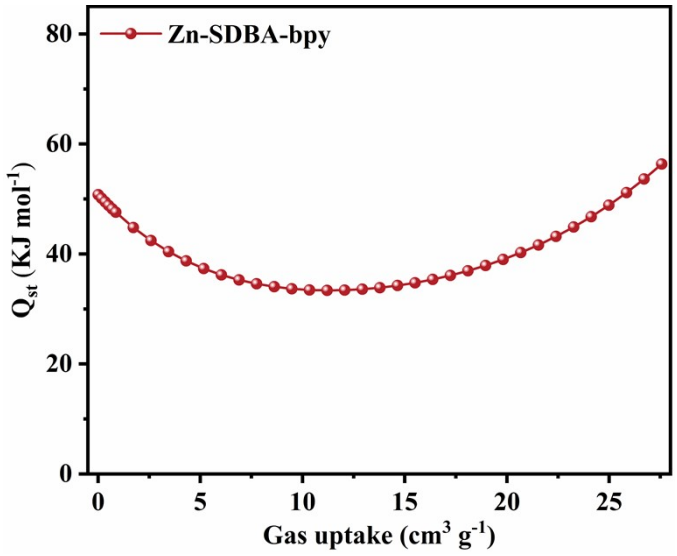

Figure S31. Q_{st} of C_2H_2 for Zn-SDBA-bpy.

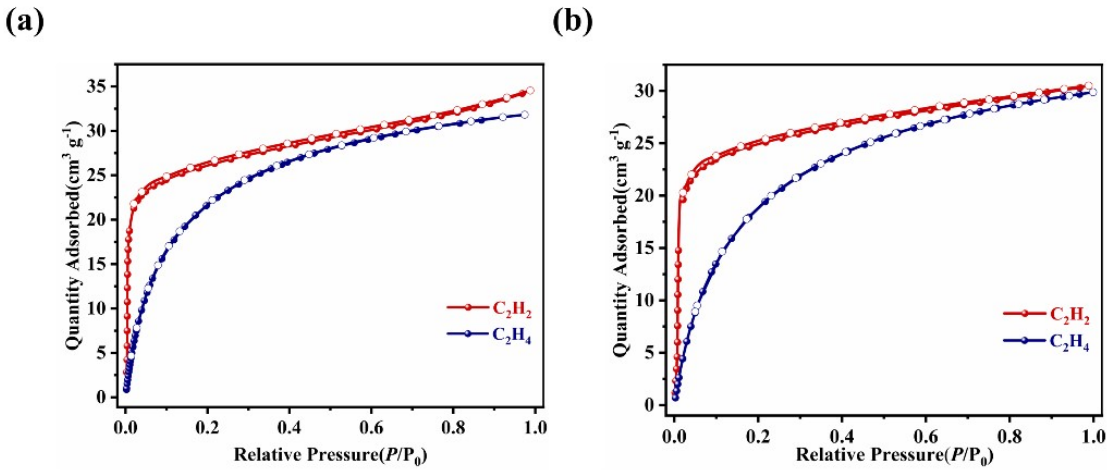

Figure S32. Adsorption isotherms of C_2H_2 and C_2H_4 on Zn-SDBA-dpe at (a) 308 K and (b) 318 K.

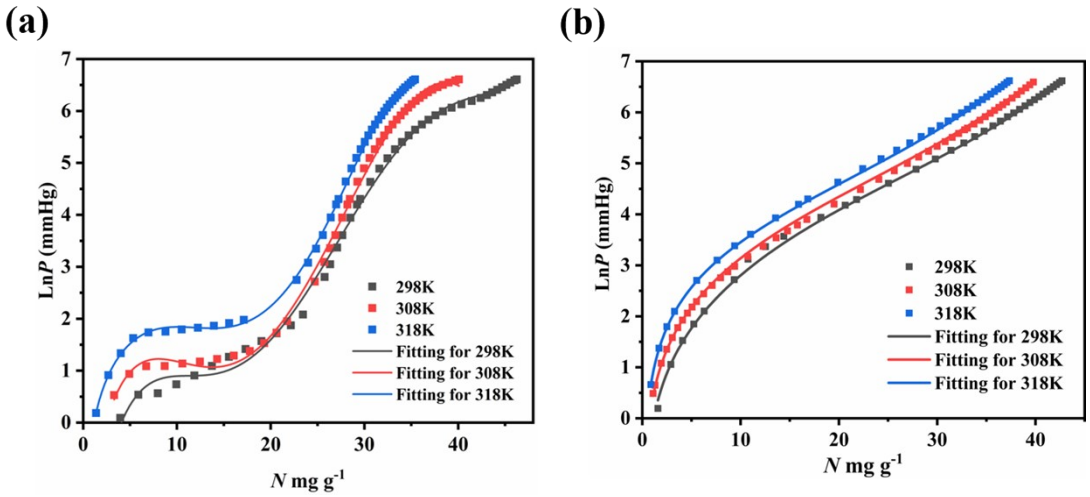

Figure S33. Virial fitting curves for (a) C_2H_2, and (b) C_2H_4 adsorption isotherms on Zn-SDBA-dpe at 298, 308, and 318 K up to 1 bar.

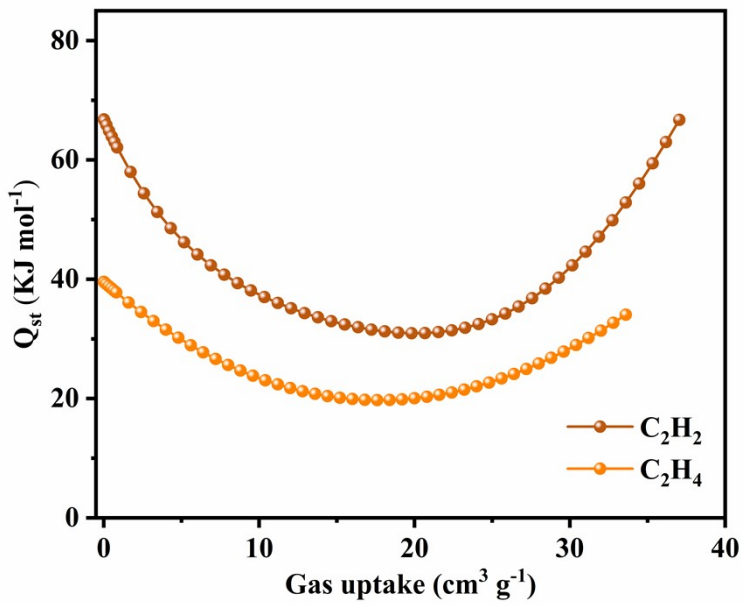

Figure S34. Q_{st} plots of C_2H_2 and C_2H_4 on Zn-SDBA-dpe.

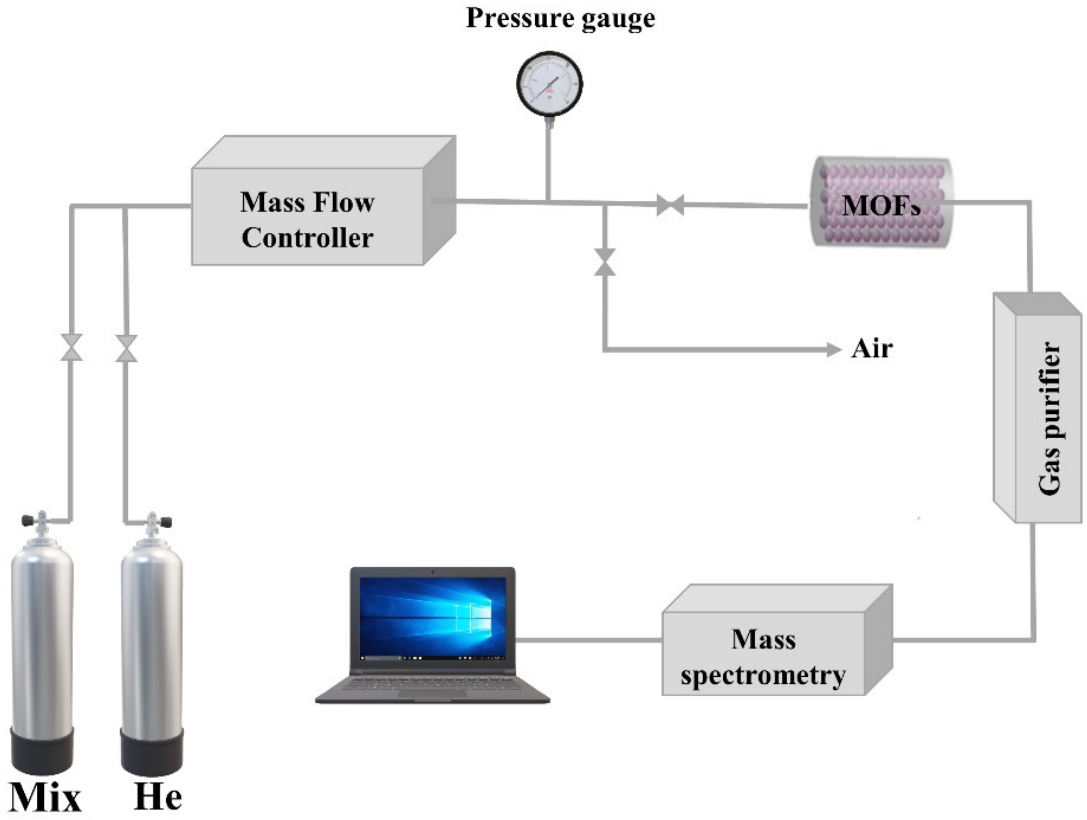

Figure S35. Breakthrough experiments apparatus.

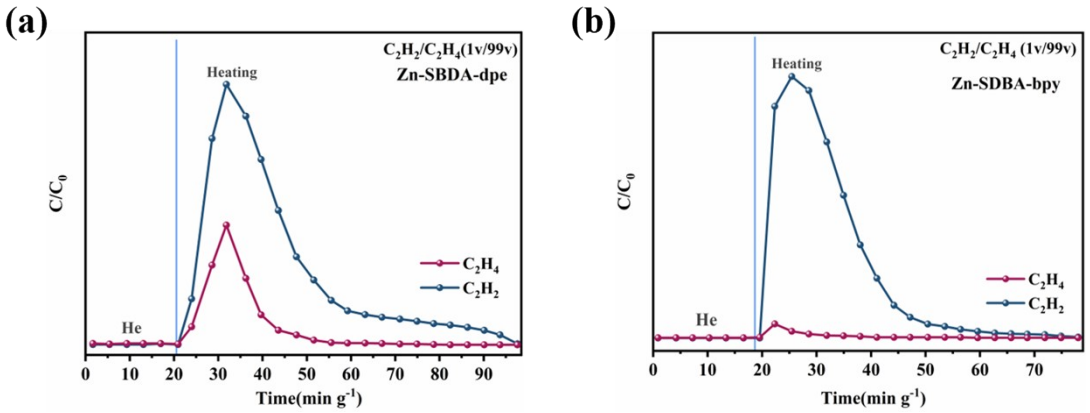

Figure S36. The desorption of desorbed C_2H_2 and C_2H_4 on (a) Zn-SDBA-dpe and (b) Zn-SDBA-bpy under a He flow rate of 2 mL min^{-1} at 373 K.

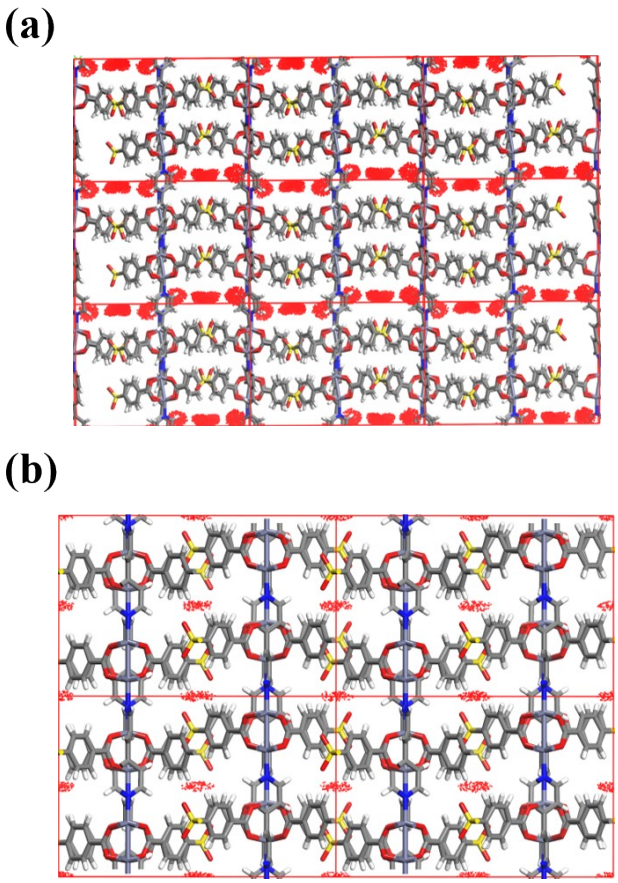

Figure S37. GCMC simulated C_2H_2 adsorption in (a) Zn-SDBA-dpe and (b) Zn-SDBA-bpy at 1.0 bar and 298 K.

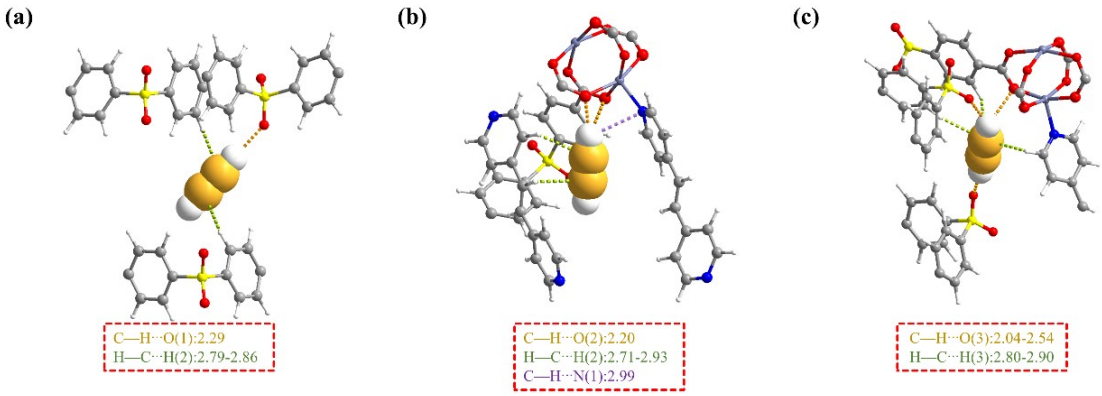

Figure S38. DFT-D calculated binding sites of C_2H_2 in Zn-SDBA-dpe.

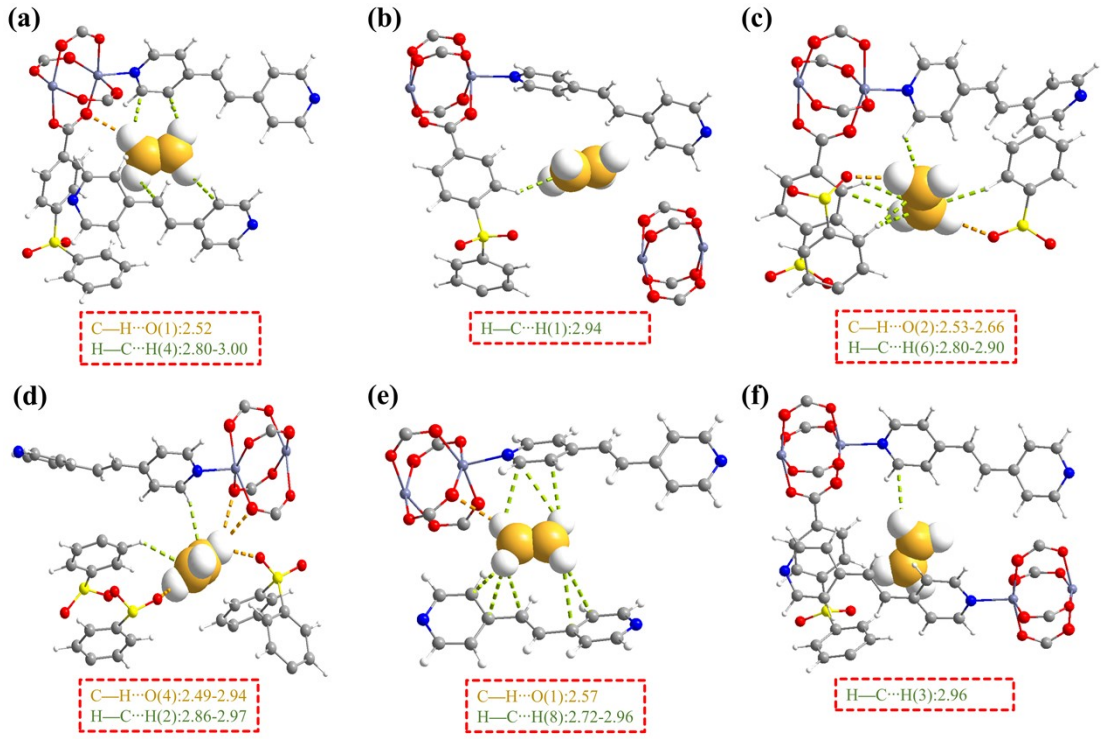

Figure S39. DFT-D calculated binding sites of C_2H_4 in Zn-SDBA-dpe.

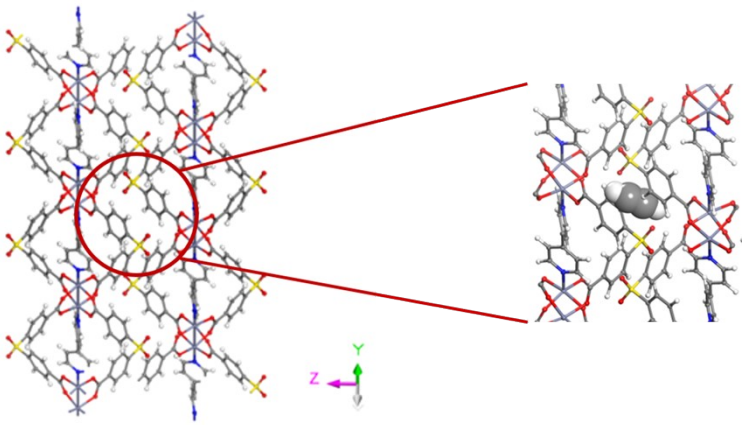

Figure S40. The diffusion of C_2H_2 molecule in the Zn-SDBA-bpy framework through the interlayer channel.

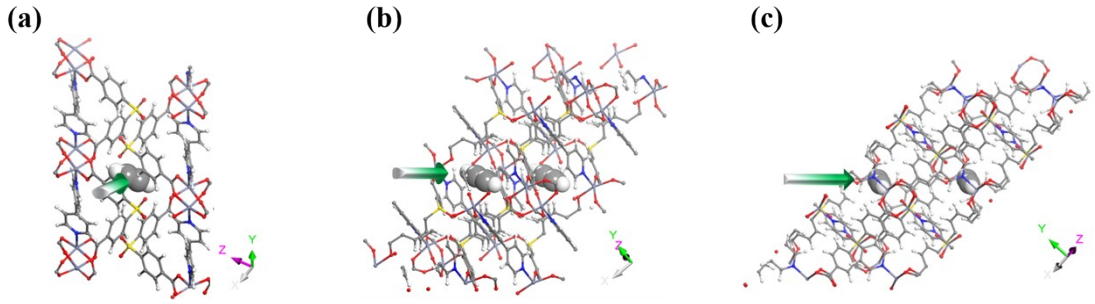

Figure S41. The diffusion pathway of C_2H_2 molecules though the interlayer into the cavity exhibited from different angles.

Supplementary Tables

Table S1. Crystallographic data for Zn-SDBA-dpe and Zn-SDBA-bpy as refined by single crystal X-ray diffraction.

Complex	**Zn-SDBA-dpe**	**Zn-SDBA-bpy**
Formula	$C_{40}H_{26}N_2O_{12}S_2Zn_2$	$C_{19}H_{12}NO_6SZn$
Mr ($g \cdot mol^{-1}$)	921.53	447.75
Crystal system	monoclinic	monoclinic
Space group	*P*21/*c*	*C*2/*c*
a (Å)	16.1271	12.8006
b (Å)	22.1251	14.0569
c (Å)	12.5264	21.5985
α/(°)	90	90
β/(°)	105.9380	90.629
γ/(°)	90	90
Z	4	4
ρ /$g \cdot cm^{-3}$	1.424	1.531
μ /mm^{-1}	2.804	1.407
F (000)	1872.0	1816
$R_1[I \geq 2\sigma(I)]$	0.0510	0.171
wR_2 (all data)	0.1391	0.2385
GOF	1.048	1.060
CCDC No.	2311766	2311765

Table S2. PXRD Rietveld refinement data of the modeled structure of activated Zn-SDBA-dpe and Zn-SDBA-bpy.

Unit cell parameters	Zn-SDBA-dpe	Zn-SDBA-bpy
Space group	*P21/c*	*C2/c*
a (Å)	16.16544	12.71917
b (Å)	22.20048	13.97307
c (Å)	12.02849	21.82633
α/(°)	90	90
β/(°)	108.082	90.71886
γ/(°)	90	90
V/(Å^3)	4103.60	3885.12
D_{calcd}/g·cm^{-3}	1.49160	1.53097
R_p	0.0503	0.0361
R_{wp}	0.0667	0.0476
R_{exp}	0.176	0.0223
GOF	3.798	2.139

Table S3. The adsorption capacity of C_2H_2 and C_2H_4, and the comparison of IAST selectivity and uptake ratio and Q_{st} at 298 K and 1.0 bar.

MOF	Uptake ($cm^3\ g^{-1}$)		IAST Selectivity		Uptake ratio	Q_{st} ($kJ \cdot mol^{-1}$) for C_2H_2	Ref.
	C_2H_2 at 1 bar	C_2H_4 at 1 bar	C_2H_2/C_2H_4[a] (1/99)(*v*/*v*)	C_2H_2/C_2H_4[a] (50/50)(*v*/*v*)	C_2H_2/C_2H_4[a] Uptake ratio		
Zn-SDBA-bpy	27.81	2.33	229.95	936.71	11.93	50.78	This work
Zn-SDBA-dpe	39.84	34.15	8.3	6.16	1.17	66.80	This work
SDMOF-1	38.08	8.51	26	15.11	4.47	47.5	[1]
UPC-22	37.41	24.19	2.7	2.6	1.55	21.1	[2]
NCU-100a	102.368	7.168	7291.3	/	14.3	60.5	[3]
UTSA-200a	81.76	14.112	6320	/	5.79	40	[4]
ZU-33	84.448	15.68	1100	/	5.39	43.6	[5]
M´MOF-3a (296	42.56	8.96	24.03	34.17	4.75	25	[6]

K)							
APPT-Cd-ClO_4^-	39.2	9.856	14.61	14.71	4.01	28.6	[7]
ZU-62-Ni	67.2	17.92	37.2	/	3.75	43	[8]
UTSA-100a (296 K)	95.65	37.18	10.72	19.55	2.57	22	[9]
ELM-12	57.344	22.4	14.8	28.7	2.56	25.4	[10]
SIFSIX-1-Cu	190.4	92.064	10.63	8.21	2.07	30	[11]
SIFSIX-3-Ni	73.92	39.2	5.03	5.98	1.89	26.3	[12]
NUM-12a	120.288	67.2	1.4	/	1.79	38.1	[13]
NOTT-300	142.01	95.87	2.17	2.3	1.48	32	[14]
NKMOF-1-Ni	60.928	47.264	44	34	1.29	60.3	[15]
Cu^I-MOF	28	23.072	1.38	1.41	1.22	21.4	[16]
ZJU-74a (296 K)	85.12	71.904	24.2	/	1.18	45	[17]

ZJU-280a (296 K)	106.176	66.08	44.5	33	1.61	50.6	[18]
TIFSIX-2-Cu-i	91.8	56	55.0	212.2	1.64	46.3	[12]
JCM-1	76.6	35.6	8.1	13.2	2.15	36.9	[19]
pacs-CoMOF-2a	121.0	62.9	11.5	/	1.92	34.2	[20]
SIFSIX-2-Cu-i	90	49.1	44.54	41.01	1.83	41.9	[11]
SIFSIX-3-Zn	81.5	50.2	8.8	13.61	1.62	31.0	[11]
UiO-66-$(CF_3)_2$	119.8	26.9	18.4	/	4.45	20.4	[21]
NbU-8 (293K)	190.0	114.9	15.3	2.01	1.65	34.6	[22]
MUF-17 (293 K)	67.4	48.2	7.1	8.7	1.40	49.5	[23]
ZNU-9	177.86	115.58	11.64	/	1.54	33.1	[24]
Co(4-DPDS)$_2$CrO$_4$	54.43	4.93	834	/	11	/	[25]
SNNU-98-Mn	111.56	56.56	/	66.1	1.97	60.2	[26]

SNNU-98-Co	72.36	54.34	2405.7	/	2.97	53.5	[26]
NTU-69	24.6	3.06	45.5	/	8.03	35.0	[27]
TIFSIX-17-Ni	73.9	7.2	/	670.9	10.26	48.3	[28]
iMOF-6C	26.9	5.6	25	10^5	4.8	38	[29]
ZUL-520-0a	107.07	10.98	504	/	9.76	/	[30]
GeFSIX-dps-Cu	95.87	3.58	/	40.1	26.75	55	[31]
ELM-11	78.4	1.34	/	/	58.33	/	[32]
ELM-13	67.2	4.03	/	/	16.67	/	[32]
CPL-1	46.37	6.94	26.75	/	6.68	40.2	[33]
UTSA-300a	68.99	0.896	27	/	77	57.6	[34]
NTU-65	75.4	1.2	/	/	62.83	/	[35]
SIFSIX-17-Ni	73.9	4.5	/	506.4	16.4	44.2	[36]

ZUL-100	118.94	61.82	175	/	1.92	65.3	[37]
TIFSIX-2-Ni-i	94.304	54.208	22.7	/	1.74	40	[38]
BSF-3	80.416	53.088	/	8	1.51	42.7	[39]
SIFSIX-DPA-Cu-i	75.59	45.4	8.7	155	1.66	46.53	[40]
FJUT-1	133.2	106.5	4.07	/	1.25	43.75	[41]
upc-80	77.28	50.44	/	4.78	1.53	20.84	[42]
Zn(dcpy)(bpe)	43.8	17.5	/	4.7	2.50	38.9	[43]
ZU-32	88.7	49.1	67	/	1.81	42.6	[5]
GeFSIX-2-Cu-i	93.41	53.54	86.3	/	1.74	50.6	[12]
ZNU-11	45.49	14.22	20.73	/	3.2	36.1	[44]

[a] Test temperature was 298 K; [b] Test temperature was 296 K; [c] Test temperature was 293 K.

Table S4. Fitting parameters of dual-site Langmuir-Freundlich isotherm model for C_2H_2 and C_2H_4 adsorption on Zn-SDBA-bpy and Zn-SDBA-dpe at 298 K and 1.0 bar.

MOFs	Gas	Saturation capacity A_1 ($mmol \cdot g^{-1}$)	Langmuir constant B_1 (kPa^{-C})	Freundlich constant C_1	Saturation capacity A_2 ($mmol \cdot g^{-1}$)	Langmuir constant B_2 (kPa^{-C})	Freundlich constant C_2	R^2
Zn-SDBA-bpy	C_2H_2	1.2405	0.08539	0.43497	0.6999	0.08306	2.79623	0.9994
	C_2H_4	0.28372	0.00731	0.86878	0.02404	5.02196E-5	2.82848	0.9999
Zn-SDBA-dpe	C_2H_2	1.00357	6.02307	1.87736	9.63826	0.00194	0.83531	0.9999
	C_2H_4	1.8964	0.12147	0.69673	0.10055	2.15342E-4	4.18925	0.9999

Table S5. The virial parameters for calculated Q_{st} of C_2H_2 on Zn-SDBA-bpy at 298 K, 308 K and 318 K up to 100 kPa.

	C_2H_2	
Viral Coefficient	Value	Standard Error
a_0	-6111.89502	379.1611
a_1	417.21321	69.97758
a_2	-30.23383	4.0715
a_3	1.07707	0.23602
a_4	-0.02246	0.00768
a_5	1.54934E-4	9.05409E-5
b_0	20.52213	1.20673
b_1	-1.02273	0.20845
b_2	0.03721	0.00686
R^2	0.9982	
Equation	$y = Ln(x)+1/T(a_0+a_1x+a_2x^2+a_3x^3+a_4x^4+a_5x^5) + (b_0+b_1x+b_2x^2)$	

Table S6. The virial parameters for calculated Q_{st} of C_2H_2 and C_2H_4 on Zn-SDBA-dpe at 298 K, 308 K and 313 K up to 100 kPa.

Viral Coefficient	C_2H_2		C_2H_4	
	Value	Standard Error	Value	Standard Error
a_0	-8087.8442	720.3420	-4759.84166	210.77895
a_1	636.52602	81.3424	218.27732	26.33818
a_2	-42.92348	3.051427	-5.09496	1.03327
a_3	1.75605	0.12244	0.00256	0.04234
a_4	-0.03724	0.00163	8.86002E-5	0.00107
a_5	2.78137E-4	2.144E-5	1.31214E-7	9.74152E-6
b_0	23.35784	2.71674	15.73292	0.67591
b_1	-1.22917	0.34144	-0.64737	0.08034
b_2	0.02968	0.00424	0.01587	0.0019
R^2	0.99925		0.99913	
Equation	$y = Ln(x)+1/T(a_0+a_1x+a_2x^2+a_3x^3+a_4x^4+a_5x^5) + (b_0+b_1x+b_2x^2)$			

REFERENCE:

1. X. Wang, H. Liu, Y. Li, X. Yang, F. Gao, X. Wang, Z. Kang, W. Fan and D. Sun, *Coord. Chem. Rev.*, 2023, **482**, 215093.
2. X. Liu, Y. Li, C. Hao, W. Fan, W. Liu, J. Liu and Y. Wang, *Inorg. Chem. Front.*, 2023, **10**, 824-831.
3. Y. Chai, X. Han, W. Li, S. Liu, S. Yao, C. Wang, W. Shi, I. da-Silva, P. Manuel, Y. Cheng, L. D. Daemen, A. J. Ramirez-Cuesta, C. C. Tang, L. Jiang, S. Yang, N. Guan and L. Li, *Science*, 2020, **368**, 1002-1006.
4. B. Li, X. Cui, D. O'Nolan, H. Wen, M. Jiang, R. Krishna, H. Wu, R. Lin, Y. Chen, D. Yuan, H. Xing, W. Zhou, Q. Ren, G. Qian, M. Zaworotko and B. Chen, *Adv. Mater.*, 2017, **29**, 1704210.
5. Z. Zhang, X. Cui, L. Yang, J. Cui, Z. Bao, Q. Yang and H. Xing, *Ind. Eng. Chem. Res.*, 2018, **57**, 7266-7274.
6. S. Xiang, Z. Zhang, C. Zhao, K. Hong, X. Zhao, D. Ding, M. Xie, C. Wu, M. Das, R. Gill, K. Thomas and B. Chen, *Nat. Commun.*, 2011, **2**, 204.
7. G. Jin, X. Niu, J. Wang, J. Ma, T. Hu and Y. Dong, *Chem. Mater.*, 2018, **30**, 7433-7437.
8. L. Yang, A. Jin, L. Ge, X. Cui and H. Xing, *Chem. Commun.*, 2019, **55**, 5001-5004.
9. T. Hu, H. Wang, B. Li, R. Krishna, H. Wu, W. Zhou, Y. Zhao, Y. Han, X. Wang, W. Zhu, Z. Yao, S. Xiang and B. Chen, *Nat. Commun.*, 2015, **6**, 7328.
10. L. Li, R. Lin, R. Krishna, X. Wang, B. Li, H. Wu, J. Li, W. Zhou and B. Chen, *J. Mater. Chem. A.*, 2017, **5**, 18984-18988.
11. X. Cui, K. Chen, H. Xing, Q. Yang, R. Krishna, Z. Bao, H. Wu, W. Zhou, X. Dong, Y. Han, B. Li, Q. Ren, M. Zaworotko and B. Chen, *Science*, 2016, **353**, 141-144.
12. J. Zheng, X. Cui, Q. Yang, Q. Ren, Y. Yang and H. Xing, *Chem. Eng. J.*, 2018, **354**, 1075-1082.
13. Q. Zhang, S. Yang, L. Zhou, L. Yu, Z. Li, Y. Zhai and T. Hu, *Inorg. Chem.*, 2021, **60**, 19328-19335.
14. S. Yang, A. Ramirez-Cuesta, R. Newby, V. Garcia-Sakai, P. Manuel, S. Callear, S. Campbell, C. Tang and M. Schröder, *Nat. Chem.*, 2015, **7**, 121-129.
15. Y. Peng, T. Pham, P. Li, T. Wang, Y. Chen, K. Chen, K. Forrest, B. Space, P. Cheng, M. Zaworotko and Z. Zhang, *Angew. Chem. Int. Ed.*, 2018, **57**, 10971-10975.
16. G. Jin, J. Wang, J. Liu, J. Ma and Y. Dong, *Inorg. Chem.*, 2018, **57**, 6218-6221.
17. J. Pei, K. Shao, J. Wang, H. Wen, Y. Yang, Y. Cui, R. Krishna, B. Li and G. Qian, *Adv. Mater.*, 2020, **32**, 1908275.

18. Q. Qian, X. Gu, J. Pei, H. Wen, H. Wu, W. Zhou, B. Li and G. Qian, *J. Mater. Chem. A.*, 2021, **9**, 9248-9255.
19. J. Lee, C. Chuah, J. Kim, Y. Kim, N. Ko, Y. Seo, K. Kim, T. Bae and E. Lee, *Angew. Chem. Int. Ed.*, 2018, **57**, 7869-7873.
20. D. Chen, C. Sun, N. Zhang, H. Si, C. Liu and M. Du, *Inorg. Chem.*, 2018, **57**, 2883-2889.
21. Y. Chen, Q. Xiong, Y. Wang, Y. Du, Y. Wang, J. Yang, L. Li and J. Li, *Chem Eng. Sci.*, 2021, **237**, 116572.
22. Q. Li, N. Wu, J. Li and D. Wu, *Inorg. Chem.*, 2020, **59**, 13005-13008.
23. O. Qazvini, R. Babarao and S. Telfer, *Chem. Mater.*, 2019, **31**, 4919-4926.
24. Y. Zhang, W. Sun, B. Luan, J. Li, D. Luo, Y. Jiang, L. Wang and B. Chen, *Angew. Chem. Int. Ed.*, 2023, **62**, e202309925.
25. F. Zheng, R. Chen, Y. Liu, Q. Yang, Z. Zhang, Y. Yang, Q. Ren and Z. Bao, *Adv. Sc.*, 2023, **10**, 2207127.
26. J. Wang, S. Fan, H. Li, X. Bu, Y. Xue and Q. Zhai, *Angew. Chem. Int. Ed.*, 2023, **62**, e202217839.
27. Y. Huang, Y. Xu, B. Zheng, Z. Wang, Q. Dong and J. Duan, *Energy & Fuels*, 2020, **34**, 11315-11321.
28. S. Mukherjee, N. Kumar, A. Bezrukov, K. Tan, T. Pham, K. Forrest, K. Oyekan, O. Qazvini, D. Madden, B. Space and M. Zaworotko, *Angew. Chem. Int. Ed.*, 2021, **60**, 10902-10909.
29. S. Dutta, S. Mukherjee, O. T. Qazvini, A. K. Gupta, S. Sharma, D. Mahato, R. Babarao and S. K. Ghosh, *Angew. Chem. Int. Ed.*, 2022, **61**, e202114132.
30. J. Zhu, T. Ke, L. Yang, Z. Bao, Z. Zhang, B. Su, Q. Ren and Q. Yang, *ACS Applied Materials & Interfaces*, 2024, **16**, 22455-22464.
31. T. Ke, Q. Wang, J. Shen, J. Zhou, Z. Bao, Q. Yang and Q. Ren, *Angew. Chem. Int. Ed.*, 2020, **59**, 12725-12730.
32. L. Li, R. Krishna, Y. Wang, X. Wang, J. Yang and J. Li, *Eur. J. Inorg. Chem.*, **2016**, 4457-4462.
33. F. Zheng, L. Guo, B. Gao, L. Li, Z. Zhang, Q. Yang, Y. Yang, B. Su, Q. Ren and Z. Bao, *ACS Applied Materials & Interfaces*, 2019, **11**, 28197-28204.
34. R. Lin, L. Li, H. Wu, H. Arman, B. Li, R. G. Lin, W. Zhou and B. Chen, *J. Am. Chem. Soc.*, 2017, **139**, 8022-8028.
35. Q. Dong, X. Zhang, S. Liu, R. B. Lin, Y. Guo, Y. Ma, A. Yonezu, R. Krishna, G. Liu, J. Duan, R. Matsuda, W. Jin and B. Chen, *Angew. Chem. Int. Ed.*, 2020, **59**, 22756-22762.
36. S. Mukherjee, N. Kumar, A. Bezrukov, K. Tan, T. Pham, K. Forrest, K. Oyekan, O.

Qazvini, D. Madden, B. Space and M. Zaworotko, *Angew. Chem. Int. Ed.*, 2021, **60**, 10902-10909.

37. J. Shen, X. He, T. Ke, R. Krishna, J. van Baten, R. Chen, Z. Bao, H. Xing, M. Dincă, Z. Zhang, Q. Yang and Q. Ren, *Nat. Commun.*, 2020, **11**.
38. M. Jiang, X. Cui, L. Yang, Q. Yang, Z. Zhang, Y. Yang and H. Xing, *Chem. Eng. J.*, 2018, **352**, 803-810.
39. Y. Zhang, J. Hu, R. Krishna, L. Wang, L. Yang, X. Cui, S. Duttwyler and H. Xing, *Angew. Chem. Int. Ed.*, 2020, **59**, 17664-17669.
40. J. You, H. Wang, T. Xiao, X. Wu, L. Zhang and C.-Z. Lu, *Chem. Eng. J.*, 2023, **477**.
41. L. Zhang, T. Xiao, X. Zeng, J. You, Z. He, C. Chen, Q. Wang, A. Nafady, A. Al-Enizi and S. Ma, *J. Am. Chem. Soc.*, 2024, **146**, 7341-7351.
42. C. Jiang, C. Hao, X. Wang, H. Liu, X. Wei, H. Xu, Z. Wang, Y. Ouyang, W. Guo, F. Dai and D. Sun, *Chem. Eng. J.*, 2023, **453**.
43. Q. Chu, S. Zhang, X. Li, P. Guo, A. Fu, B. Liu and Y. Y. Wang, *Chemistry – An Asian Journal*, 2021, **16**, 1233-1236.
44. Y. Han, Y. Jiang, J. Hu, L. Wang and Y. Zhang, *Sep. Purif. Technol.*, 2024, **332**.